ACS APPLIED MATERIALS & INTERFACES

www.acsami.org Research Article

# Role of Fluoride Doping in Low-Temperature Combustion-Synthesized $ZrO_x$ Dielectric Films

Aritra Sil, Elise A. Goldfine, Wei Huang,* Michael J. Bedzyk,* Julia E. Medvedeva,* Antonio Facchetti,* and Tobin J. Marks*

Cite This: ACS Appl. Mater. Interfaces 2022, 14, 12340−12349 Read Online

ACCESS | Metrics & More | Article Recommendations | Supporting Information

**ABSTRACT:** Zirconium oxide ($ZrO_x$) is an attractive metal oxide dielectric material for low-voltage, optically transparent, and mechanically flexible electronic applications due to the high dielectric constant ($\kappa \sim 14$−30), negligible visible light absorption, and, as a thin film, good mechanical flexibility. In this contribution, we explore the effect of fluoride doping on structure−property−function relationships in low-temperature solution-processed amorphous $ZrO_x$. Fluoride-doped zirconium oxide (F:$ZrO_x$) films with a fluoride content between 1.7 and 3.2 in atomic (at) % were synthesized by a combustion synthesis procedure. Irrespective of the fluoride content, grazing incidence X-ray diffraction, atomic-force microscopy, and UV−vis spectroscopy data indicate that all F:$ZrO_x$ films are amorphous, atomically smooth, and transparent in visible light. Impedance spectroscopy measurements reveal that unlike solution-processed fluoride-doped aluminum oxide (F:$AlO_x$), fluoride doping minimally affects the frequency-dependent capacitance instability of solution-processed F:$ZrO_x$ films. This result can be rationalized by the relatively weak Zr−F versus Zr−O bonds and the large ionic radius of $Zr^{+4}$, as corroborated by EXAFS analysis and MD simulations. Nevertheless, the performance of pentacene thin-film transistors (TFTs) with F:$ZrO_x$ gate dielectrics indicates that fluoride incorporation reduces $I$−$V$ hysteresis in the transfer curves and enhances bias stress stability versus TFTs fabricated with analogous, but undoped $ZrO_x$ films as gate dielectrics, due to reduced trap density.

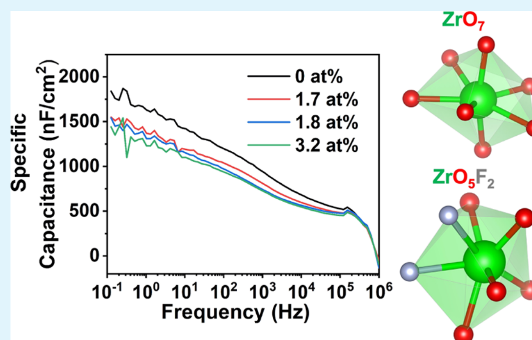


**KEYWORDS:** *high-κ dielectrics, fluoride doping, zirconium oxide, combustion synthesis, metal oxides*

Downloaded via MISSOURI UNIV SCIENCE & TECHNOLOGY on June 16, 2022 at 14:44:35 (UTC).
See https://pubs.acs.org/sharingguidelines for options on how to legitimately share published articles.

## ■ INTRODUCTION

The past decade has witnessed major advances in large-area, low-power, mechanically flexible, and wearable electronic devices enabled using thin-film transistors (TFTs) of diverse types.[1−5] In this regard, high-dielectric constant ($\kappa$) metal oxide dielectric materials such as aluminum oxide ($AlO_x$)[5−7] and zirconium oxide ($ZrO_x$)[8−12] and other unconventional dielectrics such as self-assembled nanodielectrics and composites[1,13] hold the key to TFT operation at low driving voltages.[14,15] Compared to conventional low-$\kappa$ silicon dioxide ($SiO_2$, $\kappa \sim 3.9$), high-$\kappa$ oxide materials ($\kappa \sim 8.8$−30) yield significantly higher specific capacitance values for equivalent $SiO_2$ film thickness and thereby can allow comparable source−drain currents at far lower operating voltages, essential for low-power electronics.[14,15] Furthermore, high-$\kappa$ dielectrics can circumvent the high leakage current of ultrathin $SiO_2$ (<2 nm) dielectrics, thereby extending Moore's Law.[14]

At present, most high-$\kappa$ metal oxide dielectric films are deposited using vapor-phase-based techniques such as atomic layer deposition,[16−19] sputtering,[20−22] and pulsed laser deposition.[23,24] Although vapor-phase-based methods produce high-quality films, they are time-inefficient and capital- and energy-intensive.[15] In contrast, solution-based techniques are more cost-effective and compatible with roll-to-roll manufacturing and employ less-toxic/reactive chemical precursors.[14,25,26] However, achieving complete precursor conversion to metal oxides having high chemical purity and good film densification typically requires post-film deposition annealing at temperatures of >300−400 °C.[27,28] Using lower processing temperatures for solution-processed dielectric films often results in unstable capacitance−frequency characteristics, particularly at low frequencies, due to the presence of impurities, mobile ions (e.g., $H^+$), and dipolar groups (e.g., −OH).[29−31]

Recently, this laboratory utilized fluoride doping to stabilize the capacitance at low frequencies of low-temperature solution-processed $AlO_x$ dielectric films.[32] Upon incorporation of as little as ∼3.7 atomic (at) % of fluoride in $AlO_x$, the specific capacitance of F:$AlO_x$ films, annealed at only 120 °C for 1 min

Received: November 24, 2021
Accepted: February 14, 2022
Published: March 2, 2022

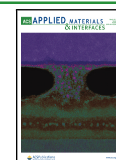


© 2022 American Chemical Society

https://doi.org/10.1021/acsami.1c22853
ACS Appl. Mater. Interfaces 2022, 14, 12340−12349

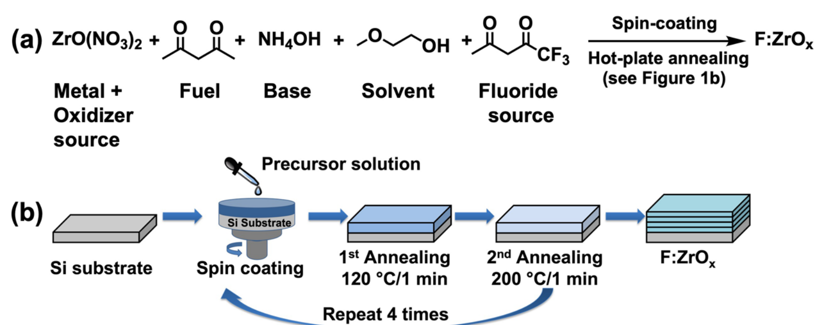


**Figure 1.** (a) Precursor chemical structures and their role in the combustion synthesis processing of F:$ZrO_x$. (b) Schematic of the spin-coating procedure for the fabrication of F:$ZrO_x$ thin films.

followed by 300 °C for 1 min, remains stable at ∼166 ± 11 nF/cm$^2$ over a wide frequency range ($10^{-1}$ to $10^4$ Hz) compared to that of the undoped $AlO_x$ samples, which changes from 781 ± 85 nF/cm$^2$ at $10^{-1}$ Hz to 104 ± 4 nF/cm$^2$ at $10^4$ Hz. As shown by solid-state NMR spectroscopy, fluoride doping achieves capacitance stabilization by generating AlOF, which strongly reduces the mobile hydrogen content, suppressing polarization mechanisms at low frequencies. When employed for TFT fabrication and when utilizing both p-type and n-type semiconductors, this capacitance stability translates into reliable TFT performance with minimum $I-V$ hysteresis, therefore enabling low-temperature solution-processed, but stable, device performance. Nevertheless, the dielectric constant of $AlO_x$ is among the lowest (6.1−9.7) of high-$\kappa$ metal oxide dielectrics.[15]

Zirconium oxide ($ZrO_x$) is a widely used high-$\kappa$ oxide dielectric with a high dielectric constant ($\kappa$ ∼ 14−30) and large band gap ($E_g$ ∼ 5.5 eV), making it an attractive candidate for low-power electronics.[15,33,34] However, to ensure its applicability in solution-processed TFTs, the frequency-dependent capacitance stability of solution-processed $ZrO_x$ films should be investigated and possibly addressed. In this contribution, we investigate structure−property−function relationships in fluoride-doped $ZrO_x$ (F:$ZrO_x$) films. Specifically, F:$ZrO_x$ films with different fluoride doping contents (0−3.2 at %) are synthesized using low-temperature combustion techniques using zirconyl nitrate ($ZrO(NO_3)_2$) and 1,1,1-trifluoroacetylacetone (FAcAc) as the Zr and fluoride sources, respectively. X-ray photoelectron spectroscopy (XPS) data corroborate fluoride incorporation and that this element ionically binds to Zr. Atomic force microscopy (AFM) and grazing incidence X-ray diffraction (GIXRD) measurements reveal that F:$ZrO_X$ films are atomically smooth and amorphous, while UV−Vis spectroscopy confirms optical transparency in the visible region, independent of the fluoride content. Impedance spectroscopic measurements reveal that unlike $AlO_x$, fluoride doping does not affect capacitance instability at low frequencies in $ZrO_x$. It will be seen that the aforementioned observations can be convincingly explained by the low bond energy of the Zr−F bonds versus Zr−O bonds and the unchanged Zr coordination upon fluoride doping, as supported by the extended X-ray absorption fine structure (EXAFS) and density function theory (DFT) + molecular dynamics (MD) simulations. Nevertheless, $F^-$ doping of $ZrO_x$ reduces hysteresis and increases bias stability in pentacene TFTs due to the reduction of interfacial charge density. Thus, this work provides an informative picture of how $F^-$ influences the structure, dielectric properties, and TFT performance in amorphous $ZrO_x$ (a-$ZrO_x$) films.

## RESULTS AND DISCUSSION

**Combustion Synthesis and Composition of Fluoride-Doped Zirconium Oxide Films.** To study the effect of fluoride doping in $ZrO_x$, solution-based combustion synthesis of metal oxides was utilized for F:$ZrO_x$ film growth. This method is known to produce oxide thin films of superior electronic properties due to the strong exotherm of the reaction lowering the required annealing time and temperature for the film growth process.[27,32,35] In this work, zirconyl nitrate ($ZrO(NO_3)_2$) was used as the Zr and oxidizer source, with acetylacetone (AcAcH) as the fuel, ammonium hydroxide ($NH_4OH$) as the base, and 2-methoxyethanol (2-Me) as the solvent (Figure 1a).[27] Note that small amounts of water [9.09% (v/v)] were used to enhance the solubility of $ZrO(NO_3)_2$ in 2-methoxyethnol (see the Experimental Section for details). After screening several fluoride sources including methyl 4,4,4-trifluoroacetylacetone (MFAcAc) and 1,1,1-trifluoroacetylacetone (FAcAc), the latter was selected as it enables higher fluoride incorporation in the $ZrO_x$ matrix (Table S1). Viscosity values of the combustion precursor solutions without and with 20 wt % FAcAc are 2.28 and 2.32 cP, respectively, which are dominated by the solvent (2-methoxyethanol). For F:$ZrO_x$ film fabrication, the precursor solutions (Figure 1a) [$ZrO(NO_3)_2$ + $x$ wt % FAcAc, $x$ = 0, 5, 10, 20] were spin-coated on n$^{++}$ Si substrates, and the resulting films were subjected to a two-step fast annealing procedure (Figure 1b) consisting of a first step that removes most of the solvent from the spin-coated film precursor, thus increasing the efficiency of heat generation in the second step.[35,36] The second step is fast and was carried out at greatly reduced annealing times and temperatures versus conventional combustion synthesis (∼0.5−1.0 h, ∼250−350 °C),[27,28] therefore enabling substantial fluoride incorporation in the $ZrO_x$ matrix.[35] Specifically, here, the annealing time and temperature were carefully optimized to 120 °C/1 min (first step) + 200 °C/1 min (second step) since increasing these parameters further dramatically reduces fluoride incorporation (Table S2). This is likely due to HF elimination by the reaction of F:$ZrO_x$ with atmospheric humidity.[36,37] A similar reaction has been documented for other metal oxides including fluoride-doped $In_2O_3$.[37,38] The entire process was repeated four times to yield ∼19 nm-thick F:$ZrO_x$ films (Figure 1b).

XPS measurements indicate that when the FAcAc quantity in the precursor solution is increased from 0 to 20 wt % [vs the total weight of $ZrO(NO_3)_2$], the fluoride content in the $ZrO_x$



https://doi.org/10.1021/acsami.1c22853
ACS Appl. Mater. Interfaces 2022, 14, 12340−12349

Table 1. Fluoride Incorporation in the F:$ZrO_x$ Films and Related Properties

| no. | FAcAc [wt %][a] | $F^-$ [at %][b] | $R_q$ [nm][c] | avg. $\rho_m$ [g/cc][d] | $E_g$ [eV][e] |
|---|---|---|---|---|---|
| 1 | 0 | 0 | 0.328 | 3.48 | 5.53 |
| 2 | 5 | 1.7 | 0.298 | 3.21 | 5.63 |
| 3 | 10 | 1.8 | 0.336 | 2.85 | 5.58 |
| 4 | 20 | 3.2 | 0.354 | 3.03 | 5.56 |

[a]Versus total weight of $ZrO(NO_3)_2$. [b]From XPS, calculated by comparing the F 1s peak with Zr 3d, O 1s, and C 1s peaks, utilizing Avantage software. [c]RMS surface roughness ($R_q$) determined by AFM. [d]Mass density ($\rho_m$) determined by XRR. [e]Direct band gap ($E_g$) determined by the Tauc plot method from UV−vis spectra.

matrices increases from 0 to 3.2 at % (Table 1 and Figure 2a). Note that addition of FAcAc to the precursor solution beyond 20 wt % does not significantly increase the fluoride concentration in the $ZrO_x$ films (e.g., 30 wt % FAcAc affords ~3.1 at % F:$ZrO_x$). This is presumably due to the solubility limit of the fluoride anion in $ZrO_x$ matrices, which is ubiquitous in various solid-state systems.[39,40] From XPS measurements, the binding energy of F 1s is ~685.15 eV. This indicates that F is present as fluoride bonded to Zr (Figure 2a) since the binding energy of ionic fluorides is 684−685.5 eV, whereas that of organic fluorides is 688−689 eV.[41] The carbon content under the optimized annealing conditions (120 °C/1 min + 200 °C/1 min) is around 2.62−3.56 at % (Table S3). Next, XPS was further employed to study metal oxide lattice formation in the F:$ZrO_x$ films. To this purpose, the O1s binding region was scanned, and the oxygen spectra were deconvoluted into three distinct oxygen environments: (1) metal oxide lattice (M−O−M) at 529.9 ± 0.1 eV; (2) metal hydroxide (M−OH) species at 531.1 ± 0.1 eV; and (3) weakly bound $CO_2$ and $H_2O$, species (M−OR) at 532.2 ± 0.1 eV.[36,42] The metal oxide lattice (M−O−M) content is associated with MO matrix densification, whereas metal hydroxide (M−OH) and weakly bound $CO_2$ and $H_2O$ species (M−OR) relate to porosity, trapping sites, and chemical impurities. Therefore, the M−O−M content ($\eta_{M-O-M}$), given by the ratio between the O 1s M−O−M area and the total O 1s peak area, is a figure of merit for the metal oxide quality. Figures 2b and S1 and Table S4 report the M−O−M, M−OH, and M−OR contents in the present F:$ZrO_x$ films. As shown in Figure 2b, the $\eta_{M-O-M}$ in undoped $ZrO_x$ is around 67.8%, consistent with other reports.[12,35,36] Upon fluoride doping, $\eta_{M-O-M}$ decreases almost linearly from 64.4% for 1.7 at % F:$ZrO_x$ to 63.9% for 1.8 at % F:$ZrO_x$ and to 62.4% for 3.2 at % F:$ZrO_x$.

**Thin-Film Morphology, Microstructure, and Optical Properties.** Next, the film microstructure and morphology were investigated by GIXRD and AFM. GIXRD reveals that under the present annealing conditions (120 °C/1 min + 200 °C/1 min), all the F:$ZrO_x$ films are amorphous (Figure 2c), which is an important characteristic of a dielectric to avoid interfacial defects in the semiconductor, minimize leakage current, and enhance dielectric strength.[43] AFM imaging (Figure 2d and Table 1) indicates that the RMS surface roughness ($R_q$) of the undoped $ZrO_x$ film is ~0.328 nm. Upon fluoride incorporation, $R_q$ remains in a narrow range of 0.298 nm for 1.7 at % F:$ZrO_x$, 0.336 nm for 1.8 at % F:$ZrO_x$, and 0.354 nm for 3.2 at % F:$ZrO_x$. Therefore, atomically smooth ($R_q$ < 1 nm) fluoride-doped $ZrO_x$ thin films were obtained utilizing combustion synthesis, which is consistent with previous combustion synthesis results.[27,32]

Next, X-ray reflectivity (XRR) measurements were carried out to assess the thickness and the mass density of the F:$ZrO_x$ films. The thickness was calculated from the first derivative of the electron density profile. The average electron density ($\rho_e$) was obtained from the area under the curve of electron density vs thickness graph and then dividing it by the film thickness. The average electron density ($\rho_e$) can be converted to mass density ($\rho_m$) by eq 1 where $M$ is the molar mass, $N_A$ is Avogadro's

$$\rho_m = \frac{\rho_e M}{N_A N_e} \quad (1)$$

number, and $N_e$ is the total number of electrons in the chemical species. Figure S2, Tables 1 and S5 report the XRR data including the electron density profile, thickness, and mass density of the F:$ZrO_x$ films. From Figure S2 and Table S5, the thickness of all F:$ZrO_x$ samples is ~18−19 nm. The resulting mass density of the undoped $ZrO_x$ film is 3.48 g/cc (Table 1), which is considerably lower than that of combustion-synthesized $ZrO_x$ (4.45 g/cc) reported in the literature and processed at a temperature of 300 °C/1 h.[27] Thus, the current

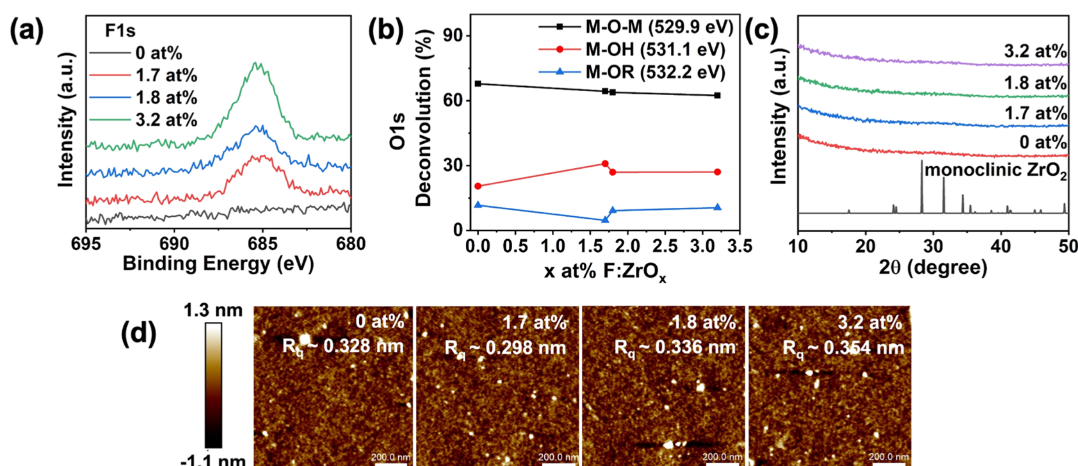


Figure 2. (a) F1s XPS spectra, (b) deconvoluted O1s environment, (c) GIXRD patterns, and (d) AFM images of the indicated $x$ at % F:$ZrO_x$ films.


https://doi.org/10.1021/acsami.1c22853
ACS Appl. Mater. Interfaces 2022, 14, 12340−12349

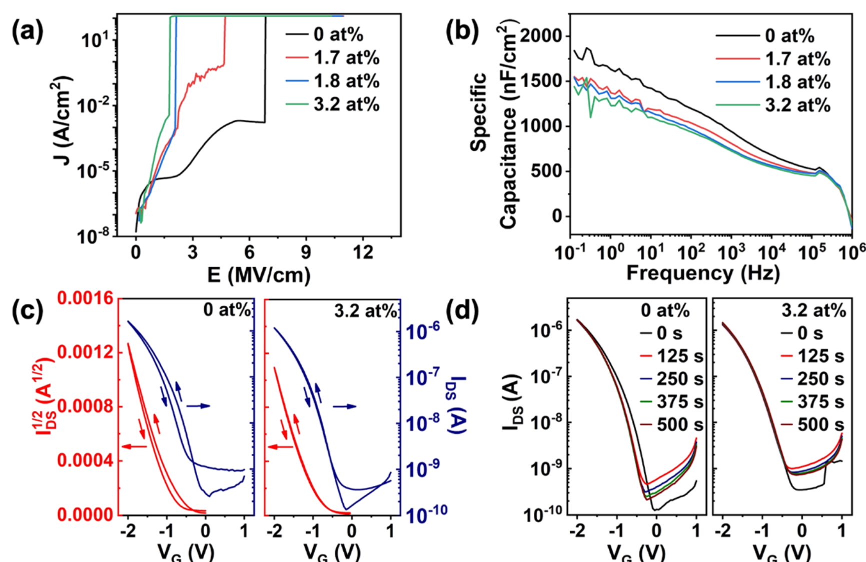


**Figure 3.** (a) Leakage current density−electric field ($J$−$E$) characteristics and (b) specific capacitance−frequency ($C$−$f$) characteristics of the indicated $x$ at % F:ZrO$_x$ dielectrics. (c) Transfer curves ($V_{DS}$ = −2 V) and (d) bias stability ($V_{DS}$ = −2 V, $V_{G,\ stress}$ = −1 V) of pentacene (P5)-TFTs based on the indicated a-$x$ at % F:ZrO$_x$ dielectrics.

procedure enables fluoride incorporation at the expense of substantial densification of the oxide matrix.[27] Upon fluoride doping, the mass density falls further to 3.21 g/cc for 1.7 at % F:ZrO$_x$, to 2.85 g/cc for 1.8 at % F:ZrO$_x$, and to 3.03 g/cc for 3.2 at % F:ZrO$_x$ (Table 1), which be explained by the MD simulation (vide infra). Regarding the changes in AFM images and XRR data between 1.7 and 1.8 at % F:ZrO$_x$, these could be rationalized by the very different amounts of reactant (AcAcF) decomposing (5 vs 10 wt %), which could very reasonably affect the film morphology and density.

Finally, the optical absorption characteristics of the F:ZrO$_x$ films were investigated by UV−vis spectroscopy (Figure S3 and Table 1). The optical transmittance spectra of F:ZrO$_x$ films in Figure S3a indicate that all samples are highly transparent (>90%) in the visible light region (380−750 nm). Therefore, fluoride doping does not significantly diminish the optical transparency of ZrO$_x$ in the visible light region, making it suitable for transparent electronics. The resulting band gap ($E_g$) values were calculated utilizing Tauc's method (Figure S3b and Table 1). The $E_g$ of ZrO$_x$ is 5.53 eV, in agreement with DFT calculations (vide infra) and literature reports.[27] Upon fluoride incorporation, $E_g$ slightly changes to 5.63 eV for 1.7 at % F:ZrO$_x$ and then falls to 5.58 eV for 1.8 at % F:ZrO$_x$ and to 5.56 eV for 3.2 at % F:ZrO$_x$ (Table 1).

**Dielectric Properties.** The dielectric properties of F:ZrO$_x$ were evaluated utilizing a metal−insulator−semiconductor (MIS) architecture where the F:ZrO$_x$ films (∼19 nm) were spin-coated on n$^{++}$ Si wafers, and the device was completed by depositing 200 × 200 $\mu$m thermally evaporated Au electrodes through a shadow mask (Figure S4). At first, the electric field (E) dependence of the leakage current density ($J$) of F:ZrO$_x$ films was investigated. As shown in Figure 3a, the breakdown electric field of undoped ZrO$_x$ is ∼6.6 MV/cm, in good agreement with literature data (∼3.5−9.5 MV/cm).[8,15,28] Upon fluoride doping, the breakdown electric field decreases from ∼4.8 MV/cm for 1.7 at % F:ZrO$_x$ to ∼2.0 MV/cm for 1.8 at % F:ZrO$_x$ and to ∼1.9 MV/cm for 3.2 at % F:ZrO$_x$ (Table S6). The leakage current density ($J$) of undoped ZrO$_x$ at 1 MV/cm is ∼4.36 × 10$^{-6}$ A/cm$^2$ (Figure 3a), and when the fluoride concentration in the ZrO$_x$ matrices increases, it falls to 5.69 × 10$^{-6}$ A/cm$^2$ for 1.7 at % F:ZrO$_x$, to 9.20 × 10$^{-6}$ A/cm$^2$ for 1.8 at % F:ZrO$_x$, and to 2.17 × 10$^{-5}$ A/cm$^2$ for 3.2 at % F:ZrO$_x$ (Table S6). Erosion of the dielectric strength upon fluoride incorporation is likely the result of the reduced M−O−M content, as assessed by XPS and lower densification as assessed by XRR (vide infra).[14,44]

Next, capacitance−frequency ($C$−$f$) plots of F:ZrO$_x$ MIS devices were measured in the frequency range from 10$^{-1}$ to 10$^6$ using an oscillating frequency of 50 mV and a bias voltage of 2 V. As shown in Figure 3b, the specific capacitance of undoped ZrO$_x$ increases almost linearly from 528 nF/cm$^2$ in the 10$^5$ Hz region to 955 nF/cm$^2$ in the 10$^3$ Hz region, to 1430 nF/cm$^2$ in the 10 Hz region, and to 1930 nF/cm$^2$ in the 10$^{-1}$ Hz region, in complete agreement with the literature report for films grown by sol−gel methods.[45] Upon fluoride doping, the present 1.7−3.2 at % F:ZrO$_x$ films exhibit a similar trend, with C increasing almost linearly from 454−484 nF/cm$^2$ in the 10$^5$ Hz region to 738−822 nF/cm$^2$ in the 10$^3$ Hz region, to 1100−1200 nF/cm$^2$ in the 10 Hz region, and to 1410−1550 nF/cm$^2$ in the 10$^{-1}$ Hz region. The dielectric constant of 0, 1.7 1.8m and 3.2 at % F:ZrO$_x$ at 1000 Hz is 28.67, 26.79, 23.48, and 24.06, respectively. Thus, F$^-$ doping does not affect $\kappa$, as expected from the $C$−$f$ plots. This result is consistent with our computational results (vide infra) since the calculated real part of the dielectric function, $\epsilon_0$, is 2.44 and 2.39 for amorphous undoped and fluoride-doped ZrO$_2$ (average of 10 realizations at optimal density), respectively. Finally, $C$−$V$ plots of $x$ at % F:ZrO$_x$ are shown in Figure S6, which also shows unchanged $C$−V characteristics with fluoride doping, in excellent agreement with $C$−$f$ data (Figure 3a).

As a control experiment, capacitance−frequency ($C$−$f$) plots of combustion-synthesized F:ZrO$_x$ films deposited at higher temperatures (120 °C/1 min + 300 °C/1 min) were measured. Note that due to increased annealing temperature, only very less (0.8 at %) fluoride ions were incorporated in the ZrO$_x$ matrices (vide supra; Table S2). Therefore, as expected, both ZrO$_x$ and 0.8 at % F:ZrO$_x$ films exhibit almost identical $C$−$f$ responses (Figure S5) due to low fluoride incorporation.


https://doi.org/10.1021/acsami.1c22853
ACS Appl. Mater. Interfaces 2022, 14, 12340−12349

Table 2. Pentacene (P5) TFT Device Performance Data Based on the Indicated a-$x$ at % F:$ZrO_x$ Gate Dielectric Films

| dielectric material | $I_{on}$ [A][a] | $I_{off}$ [A][a] | $I_{on}/I_{off}$ | $V_T$ [V][a] | $\mu$ [$cm^2 V^{-1} s^{-1}$][a] | SS [V/dec][a] | $N_{it}$ ($\times 10^{13}$) [$V^{-1} cm^{-2}$][a] |
|---|---|---|---|---|---|---|---|
| $ZrO_x$ | $1.20 \times 10^{-6} \pm 4.70 \times 10^{-7}$ | $1.98 \times 10^{-10} \pm 9.15 \times 10^{-11}$ | 103 | −0.75 ± 0.04 | 0.075 ± 0.028 | −0.29 ± 0.02 | 3.51 ± 0.25 |
| 3.2 at % F:$ZrO_x$ | $1.36 \times 10^{-6} \pm 1.79 \times 10^{-7}$ | $1.47 \times 10^{-10} \pm 3.32 \times 10^{-11}$ | $10^3$ | −0.80 ± 0.02 | 0.120 ± 0.013 | −0.30 ± 0.02 | 2.81 ± 0.18 |

[a]Average of ∼5 devices.

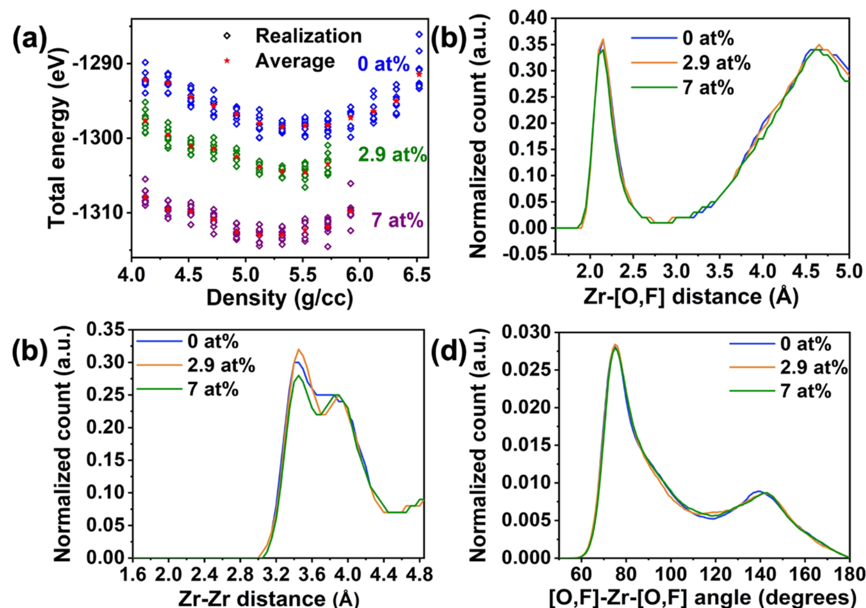


**Figure 4.** (a) Total energy of undoped and $F^-$-doped a-$ZrO_2$ as calculated from *ab initio* molecular dynamics simulations as a function of density. At least 10 MD liquid quenching realizations were obtained for each density; each diamond symbol represents total energy average over 500 MD steps at 300 K, whereas the star is the average value of 10 realizations. (b,c) Distance and (d) angle distributions for undoped and $F^-$-doped a-$ZrO_2$ as calculated from *ab initio* molecular dynamics simulations for the structures at optimal density. The results are based on 10 MD liquid quenching realizations and represent an average over 3000 MD steps at 300 K in each case.

The dielectric response of the present samples contrasts that of fluoride-doped $AlO_x$ (F:$AlO_x$) films where fluoride doping stabilizes the capacitance over a wide range of frequencies ($10^{-1}$ to $10^6$ Hz) compared to undoped $AlO_x$.[32] This result can be explained by the relatively weak Zr−F bond energy (627.1 kJ/mol) compared with that of the Zr−O bond (766.1 kJ/mol),[46] implying that F-doping replaces stronger Zr−O bonds with weaker Zr−F bonds.[46] Thus, this phenomenon acts as an impurity in the F:$ZrO_x$ system and has no effect on the $C$−$f$ responses. Note that Al−F bonds (675 kJ/mol) are stronger than Al−O bonds (501.9 kJ/mol),[46] meaning that $F^-$ doping replaces the weaker Al−O bonds with stronger Al−F bonds, which suppresses $H^+$ mobility and defects, thereby enhancing dielectric properties.[32] Compositionally, with fluoride doping in $AlO_x$, the electron density falls very little from 0.89 e/Å$^3$ ($AlO_x$) to 0.88 e/Å$^3$ (F:$AlO_x$).[32] In contrast, in F:$ZrO_x$, the electron density falls more drastically from 0.954 e/Å$^3$ for $ZrO_x$ to 0.829 e/Å$^3$ for 3.2 at % F:$ZrO_x$ (Table S5). This can be convincingly explained by MD simulation results (vide infra), and may rationalize the different $C$−$f$ responses and dielectric breakdown behaviors in F:$ZrO_x$ versus F:$AlO_x$.

**TFT Measurements.** Next, to evaluate the applicability of low-temperature combustion-synthesized F:$ZrO_x$ films as gate dielectrics in TFTs, bottom-gate top-contact TFTs with 0 at % (undoped) and 3.2 at % (largest F content) F:ZrOx dielectrics were fabricated. Since these F:$ZrO_x$ films were annealed at low temperature and metal oxide TFTs typically require higher annealing temperatures (>250 °C) and times (>20 min) for optimum device performance,[42,47] a semiconductor that can be deposited at room temperature was employed. Thus, p-type organic semiconductor pentacene (P5) films (∼30 nm thick) were vacuum-deposited at room temperature on $n^{++}$-Si/19 nm $ZrO_x$ and $n^{++}$-Si/3.2 at % F:$ZrO_x$ platforms serving as the gate electrode and the gate dielectric, respectively. Vacuum deposition at room temperature also prevents fluoride diffusion into the semiconductor. On top of the P5, 40 nm-thick gold source and drain contacts were thermally deposited through a shadow mask, yielding a device channel length ($L$) of 50 $\mu$m and width ($W$) of 1000 $\mu$m (Figure S7). Figures 3c and S8 show representative transfer and output curves, respectively. As shown in Figure S8, clear saturation behavior can be observed after −1 V $V_{DS}$. From transfer curves (Figure 3c), on-current ($I_{on}$), off-current ($I_{off}$), threshold voltage ($V_T$), carrier mobility ($\mu$), subthreshold swing (SS), and interfacial charge density ($N_{it}$) were extracted and are tabulated in Table 2. In the case of both $ZrO_x$- and F:ZrOx-based P5 TFTs, $I_{on}$ ($1.20 \times 10^{-6}$ A for $ZrO_x$ and $1.36 \times 10^{-6}$ A for 3.2 at % F:$ZrO_x$) and $I_{off}$ ($1.98 \times 10^{-10}$ A for $ZrO_x$ and $1.47 \times 10^{-10}$ A for 3.2 at % F:$ZrO_x$) remain near-identical, yielding identical $I_{on}/I_{off}$ ratios (∼$10^3$). The hole mobility increases slightly from 0.075 $cm^2$/Vs for $ZrO_x$-based P5 TFTs to 0.12 $cm^2$/Vs F:$ZrO_x$-based TFTs. Note that the mobility values of P5 TFTs obtained here are in agreement with literature values using oxide dielectrics and vapor-depositing P5 at room temperature.[32] Also, $V_T$ values


https://doi.org/10.1021/acsami.1c22853
ACS Appl. Mater. Interfaces 2022, 14, 12340−12349

Table 3. EXAFS Fitting Results of Experimental Samples[a]

| samples | CN (1st shell) | CN (2nd shell) | $R$ [Å] (1st shell) | $R$ [Å] (2nd shell) | $\sigma^2$ (1st shell) | $\sigma^2$ (2nd shell) |
|---|---|---|---|---|---|---|
| a-$ZrO_x$ | 7.68 ± 0.89 | 5.85 ± 3.85 | 2.253 ± 0.037 | 3.579 ± 0.067 | 0.0091 ± 0.0016 | 0.015 ± 0.0055 |
| a-3.2 at % F:$ZrO_x$ | 7.53 ± 0.90 | 5.92 ± 3.88 | 2.257 ± 0.038 | 3.584± 0.068 | 0.0091 ± 0.0016 | 0.015 ± 0.0065 |

[a]CN = coordination number, $R$ = bond distance, and $\sigma^2$ = mean square disorder.

increase from −0.75 V for $ZrO_x$ to −0.8 V for 3.2 at % F:$ZrO_x$ (Table 2). Interestingly, the $ZrO_x$-based P5 TFTs exhibit anticlockwise hysteresis, whereas hysteresis is negligible for the 3.2 at % F:$ZrO_x$-based P5 TFTs. This is presumably due to reduction of both interfacial charge density ($N_{it}$) at the pentacene/dielectric interface [SS ∼ −0.29 V/dec, $N_{it}$ ∼ 3.51 × $10^{13}$ $V^{-1}$ $cm^{-2}$ ($ZrO_x$); SS ∼ −0.30 V/dec, 2.8 × $10^{13}$ $V^{-1}$ $cm^{-2}$ (3.2 at % F:$ZrO_x$)],[48] calculated from SS (see eqs 3 and 4 in the Experimental Section),and reduction of bulk charge density in the dielectric layer due to fluoride doping.[48,49] As reported in the literature,[49] fluorides can form hydrogen bonds with hydroxyl groups (F···HO−M). This can passivate OH-induced trap sites, rationalizing the decrease in trap sites in the dielectric layer upon fluoride doping.[49]

Finally, the $F^-$-doped $ZrO_x$-based P5 TFTs were next subjected to a $V_G$ constant gate bias of −1 V for 125 s intervals over 500 s to test for bias stability (Figure 3d). The 3.2 at % F:$ZrO_x$-based P5 TFTs exhibit significantly improved TFT bias stability, especially after 125 s (first cycle) compared to undoped $ZrO_x$-based P5 TFTs (vide supra).

***Ab Initio* MD Simulations.** To understand the atomistic mechanisms of $F^-$ incorporation in the high-$\kappa$ oxide dielectric materials, the structural properties of undoped and $F^-$-doped a-$ZrO_2$ obtained from *ab initio* molecular dynamics liquid quenching simulations were investigated. Specifically, total energy calculations for the structures with different mass densities show that the presence of $F^-$ suppresses the total energy increase with decreasing density, Figure 4a: the energy increases by 12.1 meV/atom in a-$ZrO_2$, by 5.4 meV/atom in a-$ZrO_2$ with 2.9 at % F, and by 2.8 meV/atom in a-$ZrO_2$ with 7 at % F when the density is decreased by 8% from the optimal value in each case. Because the parabolic-like energy−density curve becomes shallower as the $F^-$ concentration increases, a large drop in density becomes energetically favorable with $F^-$ doping of a-$ZrO_2$. This finding is explained by the weaker Zr−F bonds as compared to the Zr−O bonds. At room temperature, the average time variance of the Zr−F bond length (3.3 × $10^{-3}$ $Å^2$) is more than twice larger than that for Zr−O (1.3 × $10^{-3}$ $Å^2$). These fluctuations in the Zr−F bond distances facilitate a more pronounced decrease in density in $F^-$-doped a-$ZrO_2$ as compared to $F^-$-doped amorphous $Al_2O_3$ with the opposite bond strengths for Al−O versus Al−F. This result is in agreement with the experimental mass density data obtained above from XRR data.

Figure 4b−d shows the calculated Zr−[O,F] distance and [O,F]−Zr−[O,F] angle distributions for a-$ZrO_2$ with 0, 2.9, and 7 at % F, each at optimal density (Figure 4a). Strikingly, we find that the presence of $F^-$ has no effect on the local structure of Zr. The average first-shell coordination number (CN) (bond length) changes insignificantly, from 6.77 (2.21 Å) to 6.81 (2.21 Å) and to 6.68 (2.20 Å) for 0, 2.9, and 7 at % $F^-$-doped structures, respectively. These values are calculated within the cutoff radius of 3 Å and are in agreement with those of prior computational work on a-$ZrO_2$.[50] Similarly, the Zr−Zr distance distribution varies insignificantly upon $F^-$ doping, Figure 4c. The amorphous morphology remains predominantly corner-shared (60%), whereas edge-shared and face-shared polyhedra contribute 37 and 3%, respectively, independently of the $F^-$ content. Because little changes are found for the first- and second-shell structure upon $F^-$ doping, the calculated band gap remains identical, ∼5.6 eV, for undoped and $F^-$-doped amorphous zirconia, in excellent agreement with our experimental measurements (Table 1).

Importantly, we find that the average Zr−F distance in $F^-$-doped a-$ZrO_2$, 2.25 Å, is significantly longer than the Zr−F distance in crystalline $ZrF_4$ (2.11 Å) and also slightly longer than the Zr−O distance in a-$ZrO_2$ (2.21 Å). The resulting weak Zr−F bonding along with the aforementioned strong thermal variance in the Zr−F distances in a-F:$ZrO_2$ is likely to promote dynamic changes in the morphology of the disordered lattice that make low-density $F^-$-doped configurations energetically favorable (Figure 4a), again in accordance with the observed lower densification (Table 1).

**EXAFS Measurements.** Next, intrigued by the DFT-MD simulation results and to understand the coordination environment of Zr in the a-F:$ZrO_x$ films, EXAFS measurements were carried out at the Zr $K$-edge (18 keV) on ∼19 nm-thick undoped $ZrO_x$ and 3.2 at % F:$ZrO_x$ films. For both samples, two distinct peaks were present in the pseudoradial distribution function ($p$-RDF) produced from the Fourier transform of the EXAFS absorption coefficient $\chi(k)$ (Figure S9). The first peak corresponds to the nearest neighbor Zr−O shell (1 Å < $R$ < 2 Å), while the second smaller peak corresponds to the second-nearest neighbor Zr−Zr shell (2.5 Å < $R$ < 3.5 Å). Details of EXAFS fittings are summarized in Figure S9 and Table 3.

As shown in Table 3, the first-shell CN is 7.68 and 7.53, whereas the second shell CN is 5.85 and 5.92 for undoped $ZrO_x$ and 3.2 at % F:$ZrO_x$, respectively, therefore exhibiting almost no change in CN in both shells of $ZrO_x$ upon $F^-$ doping. In addition, the bond distance ($R$) and the variances of bond distances ($\sigma^2$) for both the first and second shell of the samples are unchanged (Table 3). This result can be rationalized by the large radius of $Zr^{+4}$ (0.78 Å), which can accommodate the addition of fluoride anions without significantly changing the CN of Zr.[51] These results are in agreement with MD simulations that also indicate minimal change of the nearest and next-nearest CN in $ZrO_x$ matrices with fluoride doping.

## CONCLUSIONS

This contribution reports the first detailed investigation of $F^-$ doping as a means to clarify structure−property−function relationships in a-F:$ZrO_x$ films. The precursor chemistry, fluoride source, and annealing conditions were thoroughly optimized to enable significant fluoride incorporation (0.0−3.2 at %) in the $ZrO_x$ matrix. The F 1s binding energies from XPS reveal that the organic precursor is fully thermolyzed and the fluoride ion is ionically bounded to $Zr^{+4}$. AFM, GIXRD, XRR, and UV−vis spectroscopy studies confirm that atomically smooth, amorphous, visible light-transparent F:$ZrO_x$ samples are produced via combustion synthesis. Impedance spectros-


https://doi.org/10.1021/acsami.1c22853
ACS Appl. Mater. Interfaces 2022, 14, 12340−12349

copy measurements indicate that fluoride doping does not significantly affect capacitance instability at low frequencies in low-temperature solution-processed F:$ZrO_x$ dielectric films. This seminal observation can be rationalized by the low bond energy of Zr−F compared to Zr−O and the large ionic radius of $Zr^{+4}$, further supported by EXAFS and MD simulations. Furthermore, pentacene TFTs fabricated with F:$ZrO_x$ gate dielectric films reveal that fluoride doping reduces $I-V$ hysteresis compared to $ZrO_x$ dielectrics due to the reduction of trap charge density, demonstrating its applicability in TFT performance optimization. This is the first study investigating anion doping in the structure−function relationship in application-relevant high-κ $ZrO_x$, paving the way for high-performing optoelectronic devices in future.

## EXPERIMENTAL SECTION

**Combustion Precursor Solution Preparation.** All chemicals were purchased from Sigma-Aldrich and Alfa-Aesar and were used without further purification. Exactly 346.86 mg of $ZrO(NO_3)_2$ was dissolved in 3.0 mL of water [9.09% (v/v)] and sonicated for 30 min. To this, 30 mL of 2-methoxyethanol was added, followed by the addition of 150 μL of acetylacetone and 67.5 μL of ammonium hydroxide solution (14.5 M), and the resulting 0.05 M solution was stirred for 12−14 h. Then, the resulting solution was filtered using 0.45 μm PVDF filters. Approximately 1 h prior to spin coating, the fluoride precursor 1,1,1-trifluoro-2,4-pentanedione (FAcAc) in 0, 5, 10, and 20 wt % to the total weight of $ZrO(NO_3)_2$ was added to 5 mL of the abovementioned precursor solutions. The resulting solution was filtered again utilizing 0.20 μm PTFE filters before spin coating.

Solution viscosity was measured at 25 °C, 60 rpm, utilizing a Brookfield viscometer.

**Capacitor and Transistor Fabrication and Electrical Characterization.** $n^{++}$-Si wafers were used as the gate electrode. Before spin coating, the substrates were cleaned ultrasonically in a 1:1 mixture of isopropyl alcohol and acetone three times (10 min each), followed by 5 min in an $O_2$ plasma. Then, the filtered precursor solutions (using a 0.2 μm syringe PTFE membrane) were spin-coated at 3500 rpm for 30 s and then annealed on a hot plate at 120 °C for 1 min followed by 200 °C for 1 min (relative humidity ∼ 33%). This process was repeated four times to achieve the desired thickness (∼18−19 nm). Finally, 40 nm Au electrodes (200 μm × 200 μm) were thermally evaporated utilizing a shadow mask.

Impedance characterization was performed under ambient conditions in the dark on a custom probe station using an Agilent 1500 semiconductor parameter analyzer or a Bio-Logic SP-150 analyzer.

For TFT fabrication, $n^{++}$-Si wafer/($F^-$-doped) $ZrO_x$ were used as the gate electrode and dielectrics, respectively. On top of that, a 30 nm pentacene (P5) film was vacuum-deposited at room temperature at a rate of ∼0.02−0.03 nm $s^{-1}$ (∼5 × $10^{-6}$ Torr). Then, 40 nm Au source/drain electrodes were thermally evaporated to form a channel length of 50 μm and channel width of 1000 μm utilizing shadow masks. TFT characterization was performed under ambient light and atmosphere on a custom probe station using an Agilent 1500 semiconductor parameter analyzer. Electron mobility (μ) was calculated in the saturation regime using the following equation

$$I_{DS} = \frac{\mu CW(V_G - V_T)^2}{2L} \tag{2}$$

Here, $C$ is the capacitance per unit area of the dielectric layer, $V_T$ is the threshold voltage, $V_G$ is the gate voltage, $I_{DS}$ is the source−drain current, and $W$ and $L$ are the channel width and length, respectively.

SS was calculated using the following equation[52]

$$SS = \frac{dV_G}{d\log_{10} I_{SD}} \tag{3}$$

Interfacial charge density ($N_{it}$) was calculated using the following equation[53]

$$SS = \ln 10 \frac{kT}{q}\left(1 + \frac{qN_{it}}{C_i}\right) \tag{4}$$

Here, $k$ is the Boltzmann constant, $T$ is the absolute temperature ($T$ = 298 K here), $q$ is the charge of the carrier (1.602 × $10^{-19}$ C), and $C_i$ is capacitance per unit area of the dielectric.

**Oxide Film Characterization.** AFM data were acquired using a Bruker Dimension FastScan atomic force microscope in the tapping mode.

GIXRD and XRR measurements were carried out with a Rigaku SmartLab thin-film diffraction workstation using a high intensity 9 kW copper rotating anode X-ray source, which is coupled to a multilayer optic. XRR data were fit with the Igor-based MOTOFIT package. UV−vis samples were prepared on quartz substrates, and the UV−vis spectra were acquired using a PerkinElmer LAMBDA 1050 UV−vis−NIR spectrophotometer. XPS analyses were performed on a Thermo Scientific ESCALAB 250Xi at a base pressure of 4.5 × $10^{-10}$ mbar. Spectra were obtained after the surface of the film was etched with an Ar etch gun for 20 s.

Extended X-ray absorption fine structure (EXAFS) measurements were performed at the beamline 5BM-D at the Advanced Photon Source at Argonne National Laboratory. Data were collected at the Zr $K$-edge (18 keV). ∼19 nm film samples of amorphous $ZrO_x$ and $F^-$-doped $ZrO_x$ on quartz substrates were measured in the fluorescence mode. Crystalline $ZrO_2$ powder was used as a reference. The normalized linear EXAFS absorption coefficient $\chi(k)$ was fit by the equation

$$\chi(k) = \sum_i \frac{S_0^2 N_i f_i(k)}{kR_i^2} \sin[2kR_i + \delta(k)] e^{-\frac{2R_i}{\lambda(k)}} e^{-2k^2\sigma_{R_i}^2} \tag{5}$$

where $S_0^2$ is the intrinsic loss factor, $\lambda(k)$ is the electron mean free path, $N_i$ and $R_i$ are the CN and bond distance of the $i$th shell of the absorbing atom, respectively, $f_i(k)$ and $\delta(k)$ are the backscattering amplitude and the phase shift, respectively, and $e^{-2k^2\sigma_{R_i}^2}$ is the Debye−Waller factor—a measure of the structural disorder or variation in $R_i$. The CN, bond distances, and Debye−Waller factors were refined for the nearest neighbor (O) and second-nearest neighbor (Zr) shells to determine the effect of fluoride doping on the local structure. Data reduction and analysis were performed using the Demeter software package.[54] The initial model was obtained using FEFF simulations based on crystalline $ZrO_2$. The intrinsic loss factor ($S_0^2$ = 0.98) was determined from the fit to the crystalline reference sample with the CN fixed to the expected value for $ZrO_2$. Fittings were carried out over the $R$-range 1.1−3.5 Å using data in the $k$-range of 3−11 $Å^{-1}$. Fitting was done in $R$-space, and a $k$-weight of 2 and 3 was used.

**Computational Approach.** A-$ZrO_2$ structures with and without $F^-$ doping were calculated using the Vienna Ab Initio Simulation Package (VASP).[55−58] The calculations are based on DFT[59,60] with periodic boundary conditions and use the PBE functional[61,62] within the projector augmented-wave method.[63,64] To obtain amorphous structures, we employed the *ab initio* molecular dynamics (MD) liquid quenching approach as implemented in VASP. An initial $Zr_{46}O_{92}$ structure with a crystalline density of 5.68 g/$cm^3$ was melted at 5000 K to eliminate any crystalline memory. For F:$ZrO_2$, fluoride atoms were randomly introduced into the supercell, and the number of oxygen atoms was adjusted to zero maintain charge neutrality, resulting in $Zr_{46}O_{90}F_4$ (2.9 at % F) and $Zr_{46}O_{87}F_{10}$ (7 at % F) configurations. The structures had additional melting at 5000 K for 10 ps to randomize the multicomponent configuration and stabilize the total energy. Next, each structure was rapidly quenched to 100 K at 200 K/ps rate. An energy cutoff of 260 eV and single Γ-point were used during melting and quenching processes. Finally, each structure was equilibrated at 300 K for 6 ps with a cutoff energy of 400 eV. All MD simulations were carried out in the *NVT* ensemble with a Nose−Hoover thermostat using an integration time step of 2 fs. For an


https://doi.org/10.1021/acsami.1c22853
ACS Appl. Mater. Interfaces 2022, 14, 12340−12349

accurate structural analysis of the simulated amorphous oxides (distance and angle distributions), the room temperature structures were used.

To determine the supercell density, at least 10 melt−quench cycles were performed for each density value that ranged from 4.12 to 6.52 g/cm$^3$ for undoped a-$ZrO_2$. Based on the total energy density calculations, the optimal density was found to be 5.32 g/cm$^3$ for undoped amorphous zirconia, which is about 6% lower than crystalline density.

Finally, the atomic configurations obtained from the *ab initio* MD simulations were optimized within DFT using the PBE functional. For the optimization, a cutoff energy of 500 eV and the $4 \times 4 \times 4$ Γ-centered *k*-point were used; the atomic positions were relaxed until the Hellmann−Feynman force on each atom was below 0.01 eV/Å. The electronic and optical properties of the optimized amorphous zirconia were calculated using the hybrid Heyd−Scuseria−Ernzerhof (HSE06) approach[65,66] with a mixing parameter of 0.25 and a screening parameter $\alpha$ of 0.2 Å$^{-1}$. Optical absorption was derived from the frequency-dependent dielectric function, $\varepsilon(\omega) = \varepsilon_1(\omega) + i\varepsilon_2(\omega)$, calculated within independent particle approximation in VASP. The imaginary part, $\varepsilon_2(\omega)$, is related to the optical absorption at a given frequency, $\omega$, and is determined based on the electronic transitions of the hybrid functional solution. The real part of the complex dielectric function is obtained using Kramers−Kronig relations. The resulting atomic structures were plotted using VESTA software.[67]

## ASSOCIATED CONTENT

### Supporting Information

The Supporting Information is available free of charge at https://pubs.acs.org/doi/10.1021/acsami.1c22853.

AFM, XRR plots and data, TFT architecture, bias stress data, MD simulations, UV−Vis data, and XPS data (PDF)

## AUTHOR INFORMATION

### Corresponding Authors

**Wei Huang** − *Department of Chemistry and the Materials Research Center, Northwestern University, Evanston, Illinois 60208, United States; School of Automation Engineering, University of Electronic Science and Technology of China (UESTC), Chengdu, Sichuan 611731, China;* orcid.org/0000-0002-0973-8015; Email: weihuang@northwestern.edu

**Michael J. Bedzyk** − *Department of Materials Science and Engineering and the Materials Research Center, Northwestern University, Evanston, Illinois 60208, United States;* orcid.org/0000-0002-1026-4558; Email: bedzyk@northwestern.edu

**Julia E. Medvedeva** − *Department of Physics, Missouri University of Science and Technology, Rolla, Missouri 65409, United States;* orcid.org/0000-0001-7142-1644; Email: juliaem@mst.edu

**Antonio Facchetti** − *Department of Chemistry and the Materials Research Center, Northwestern University, Evanston, Illinois 60208, United States; Flexterra Inc., Skokie, Illinois 60077, United States;* orcid.org/0000-0002-8175-7958; Email: a-facchetti@northwestern.edu

**Tobin J. Marks** − *Department of Chemistry and the Materials Research Center, Northwestern University, Evanston, Illinois 60208, United States;* orcid.org/0000-0001-8771-0141; Email: t-marks@northwestern.edu

### Authors

**Aritra Sil** − *Department of Chemistry and the Materials Research Center, Northwestern University, Evanston, Illinois 60208, United States*

**Elise A. Goldfine** − *Department of Materials Science and Engineering and the Materials Research Center, Northwestern University, Evanston, Illinois 60208, United States*

Complete contact information is available at: https://pubs.acs.org/10.1021/acsami.1c22853

### Notes

The authors declare no competing financial interest.

## ACKNOWLEDGMENTS

We thank the Northwestern U. MRSEC grant NSF-DMR 1720139 for support of this research. J.E.M. thanks NSF-DMREF grants 1729779 and DMR-1842467 for support and NSF-MRI grant OAC-1919789 for computational facilities. This work made use of the EPIC, Keck-II, and/or SPID facility(ies) of Northwestern University's NU*ANCE* Center, which has received support from the Soft and Hybrid Nanotechnology Experimental (SHyNE) Resource (NSF ECCS-1542205); the MRSEC program (NSF DMR-1720139) at the Materials Research Center; the International Institute for Nanotechnology (IIN); the Keck Foundation; and the State of Illinois, through the IIN. XRR measurements used the Jerome B. The Cohen X-Ray Diffraction Facility also supported by the NSF MRSEC and SHyNE resource. This work used the 5-BM-D beamline of the DuPont-Northwestern-Dow Collaborative Access Team (DND-CAT) located at Sector 5 of the Advanced Photon Source (APS). DND-CAT is supported by Northwestern University (NU), E.I. DuPont de Nemours & Co., and the Dow Chemical Company. Special thanks to Qing Ma for EXAFS measurements conducted during remote operation of the APS. This research used resources of the APS, a U.S. Department of Energy (DOE) Office of Science User Facility operated for the DOE Office of Science by Argonne National Laboratory under contract no. DE-AC02-06CH11357.

## ABBREVIATIONS

XPS, X-ray photoelectron spectroscopy
AFM, atomic force microscopy
GIXRD, grazing incidence X-ray diffraction
XRR, X-ray reflectivity
TFT, thin-film transistor
MD, molecular dynamics
DFT, density functional theory
EXAFS, extended X-ray absorption fine structure
UV/Vis/NIR, ultraviolet/visible/near infrared
soln., solution
w/o, without
at %, atom %
vs, versus
wt %, weight %

## REFERENCES

(1) Stallings, K.; Smith, J.; Chen, Y.; Zeng, L.; Wang, B.; Di Carlo, G.; Bedzyk, M. J.; Facchetti, A.; Marks, T. J. Self-Assembled Nanodielectrics for Solution-Processed Top-Gate Amorphous Igzo Thin-Film Transistors. *ACS Appl. Mater. Interfaces* **2021**, *13*, 15399.

(2) Wang, B.; Thukral, A.; Xie, Z.; Liu, L.; Zhang, X.; Huang, W.; Yu, X.; Yu, C.; Marks, T. J.; Facchetti, A. Flexible and Stretchable

Metal Oxide Nanofiber Networks for Multimodal and Monolithically Integrated Wearable Electronics. *Nat. Commun.* **2020**, *11*, 2405.
(3) Myny, K. The Development of Flexible Integrated Circuits Based on Thin-Film Transistors. *Nat. Electron.* **2018**, *1*, 30.
(4) Lei, T.; Shao, L.-L.; Zheng, Y.-Q.; Pitner, G.; Fang, G.; Zhu, C.; Li, S.; Beausoleil, R.; Wong, H.-S. P.; Huang, T.-C.; Cheng, K.-T.; Bao, Z. Low-Voltage High-Performance Flexible Digital and Analog Circuits Based on Ultrahigh-Purity Semiconducting Carbon Nanotubes. *Nat. Commun.* **2019**, *10*, 2161.
(5) Yu, B.-S.; Jeon, J.-Y.; Kang, B.-C.; Lee, W.; Kim, Y.-H.; Ha, T.-J. Wearable 1 V Operating Thin-Film Transistors with Solution-Processed Metal-Oxide Semiconductor and Dielectric Films Fabricated by Deep Ultra-Violet Photo Annealing at Low Temperature. *Sci. Rep.* **2019**, *9*, 8416.
(6) Park, S.-J.; Jeon, J.-Y.; Kang, B.-C.; Ha, T.-J. Wearable Temperature Sensors Based on Lanthanum-Doped Aluminum-Oxide Dielectrics Operating at Low-Voltage and High-Frequency for Healthcare Monitoring Systems. *Ceram. Int.* **2021**, *47*, 4579.
(7) Cai, W.; Zhang, J.; Wilson, J.; Song, A. Low-Voltage, Full-Swing Ingazno-Based Inverters Enabled by Solution-Processed, Ultra-Thin Alxoy. *IEEE Electron Device Lett.* **2019**, *40*, 1285.
(8) Islam, M. M.; Saha, J. K.; Hasan, M. M.; Kim, J.; Bukke, R. N.; Ali, A.; Jang, J. Spray Pyrolyzed High K Zirconium Aluminum Oxide Dielectric for High Performance Metal-Oxide Thin Film Transistors for Low Power Displays. *Adv. Mater. Interfaces* **2021**, *8*, 2100600.
(9) Liu, A.; Liu, G. X.; Zhu, H. H.; Xu, F.; Fortunato, E.; Martins, R.; Shan, F. K. Fully Solution-Processed Low-Voltage Aqueous In2o3 Thin-Film Transistors Using an Ultrathin Zro(X) Dielectric. *ACS Appl. Mater. Interfaces* **2014**, *6*, 17364.
(10) Wang, Z.; Meng, Y.; Cui, Y.; Fan, C.; Liu, G.; Shin, B.; Feng, D.; Shan, F. Low-Voltage and High-Performance Field-Effect Transistors Based on Znxsn1-Xo Nanofibers with a Zrox Dielectric. *Nanoscale* **2018**, *10*, 14712.
(11) Zhu, L.; He, G.; Lv, J.; Fortunato, E.; Martins, R. Fully Solution-Induced High Performance Indium Oxide Thin Film Transistors with Zrox High-K Gate Dielectrics. *RSC Adv.* **2018**, *8*, 16788.
(12) Jeong, Y. J.; Yun, D.-J.; Nam, S.; Suh, E. H.; Park, C. E.; An, T. K.; Jang, J. Photo-Patternable High-K Zrox Dielectrics Prepared Using Zirconium Acrylate for Low-Voltage-Operating Organic Complementary Inverters. *Org. Electron.* **2016**, *33*, 40.
(13) Chen, Y.; Zhuang, X.; Goldfine, E. A.; Dravid, V. P.; Bedzyk, M. J.; Huang, W.; Facchetti, A.; Marks, T. J. Printable Organic-Inorganic Nanoscale Multilayer Gate Dielectrics for Thin-Film Transistors Enabled by a Polymeric Organic Interlayer. *Adv. Funct. Mater.* **2020**, *30*, 2005069.
(14) Liu, A.; Zhu, H.; Sun, H.; Xu, Y.; Noh, Y. Y. Solution Processed Metal Oxide High-Kappa Dielectrics for Emerging Transistors and Circuits. *Adv. Mater.* **2018**, *30*, No. e1706364.
(15) Wang, B.; Huang, W.; Chi, L.; Al-Hashimi, M.; Marks, T. J.; Facchetti, A. High- K Gate Dielectrics for Emerging Flexible and Stretchable Electronics. *Chem. Rev.* **2018**, *118*, 5690.
(16) Leskelä, M.; Ritala, M. Atomic Layer Deposition (Ald): From Precursors to Thin Film Structures. *Thin Solid Films* **2002**, *409*, 138.
(17) Ritala, M.; Kukli, K.; Rahtu, A.; Räisänen, P. I.; Leskelä, M.; Sajavaara, T.; Keinonen, J. Atomic Layer Deposition of Oxide Thin Films with Metal Alkoxides as Oxygen Sources. *Science* **2000**, *288*, 319.
(18) Aoki, Y.; Kunitake, T. Solution-Based Fabrication of High-K Gate Dielectrics for Next-Generation Metal-Oxide Semiconductor Transistors. *Adv. Mater.* **2004**, *16*, 118.
(19) Liu, J.; Li, J.; Wu, J.; Sun, J. Structure and Dielectric Property of High-K Zro2 Films Grown by Atomic Layer Deposition Using Tetrakis(Dimethylamido)Zirconium and Ozone. *Nanoscale Res. Lett.* **2019**, *14*, 154.
(20) Zhou, Y.; Kojima, N.; Sasaki, K. Growth and Dielectric Properties of Tetragonal Zro2films by Limited Reaction Sputtering. *J. Phys. D: Appl. Phys.* **2008**, *41*, 175414.
(21) Musil, J.; Baroch, P.; Vlček, J.; Nam, K. H.; Han, J. G. Reactive Magnetron Sputtering of Thin Films: Present Status and Trends. *Thin Solid Films* **2005**, *475*, 208.
(22) Liang, L. Y.; Cao, H. T.; Liu, Q.; Jiang, K. M.; Liu, Z. M.; Zhuge, F.; Deng, F. L. Substrate Biasing Effect on the Physical Properties of Reactive Rf-Magnetron-Sputtered Aluminum Oxide Dielectric Films on Ito Glasses. *ACS Appl. Mater. Interfaces* **2014**, *6*, 2255.
(23) Zhu, J.; Li, T. L.; Pan, B.; Zhou, L.; Liu, Z. G. Enhanced Dielectric Properties of Zro2thin Films Prepared in Nitrogen Ambient by Pulsed Laser Deposition. *J. Phys. D: Appl. Phys.* **2003**, *36*, 389.
(24) Geng, G. Z.; Liu, G. X.; Shan, F. K.; Liu, A.; Zhang, Q.; Lee, W. J.; Shin, B. C.; Wu, H. Z. Improved Performance of Ingazno Thin-Film Transistors with Ta2o5/Al2o3 Stack Deposited Using Pulsed Laser Deposition. *Curr. Appl. Phys.* **2014**, *14*, S2.
(25) Xu, W.; Li, H.; Xu, J.-B.; Wang, L. Recent Advances of Solution-Processed Metal Oxide Thin-Film Transistors. *ACS Appl. Mater. Interfaces* **2018**, *10*, 25878.
(26) Park, J. W.; Kang, B. H.; Kim, H. J. A Review of Low-Temperature Solution-Processed Metal Oxide Thin-Film Transistors for Flexible Electronics. *Adv. Funct. Mater.* **2019**, *30*, 1904632.
(27) Wang, B.; Yu, X.; Guo, P.; Huang, W.; Zeng, L.; Zhou, N.; Chi, L.; Bedzyk, M. J.; Chang, R. P. H.; Marks, T. J.; Facchetti, A. Solution-Processed All-Oxide Transparent High-Performance Transistors Fabricated by Spray-Combustion Synthesis. *Adv. Electron. Mater.* **2016**, *2*, 1500427.
(28) Park, S.; Kim, C.-H.; Lee, W.-J.; Sung, S.; Yoon, M.-H. Sol-Gel Metal Oxide Dielectrics for All-Solution-Processed Electronics. *Mater. Sci. Eng., R* **2017**, *114*, 1.
(29) Banger, K.; Warwick, C.; Lang, J.; Broch, K.; Halpert, J. E.; Socratous, J.; Brown, A.; Leedham, T.; Sirringhaus, H. Identification of Dipole Disorder in Low Temperature Solution Processed Oxides: Its Utility and Suppression for Transparent High Performance Solution-Processed Hybrid Electronics. *Chem. Sci.* **2016**, *7*, 6337.
(30) Heo, J.; Choi, S.; Jo, J.-W.; Kang, J.; Park, H.-H.; Kim, Y.-H.; Park, S. Frequency-Stable Ionic-Type Hybrid Gate Dielectrics for High Mobility Solution-Processed Metal-Oxide Thin-Film Transistors. *Materials* **2017**, *10*, 612.
(31) Balakrishna Pillai, P.; Kumar, A.; Song, X.; De Souza, M. M. Diffusion-Controlled Faradaic Charge Storage in High-Performance Solid Electrolyte-Gated Zinc Oxide Thin-Film Transistors. *ACS Appl. Mater. Interfaces* **2018**, *10*, 9782.
(32) Zhuang, X.; Patel, S.; Zhang, C.; Wang, B.; Chen, Y.; Liu, H.; Dravid, V. P.; Yu, J.; Hu, Y.-Y.; Huang, W.; Facchetti, A.; Marks, T. J. Frequency-Agile Low-Temperature Solution-Processed Alumina Dielectrics for Inorganic and Organic Electronics Enhanced by Fluoride Doping. *J. Am. Chem. Soc.* **2020**, *142*, 12440.
(33) Zhu, C.; Liu, A.; Liu, G.; Jiang, G.; Meng, Y.; Fortunato, E.; Martins, R.; Shan, F. Low-Temperature, Nontoxic Water-Induced High-K Zirconium Oxide Dielectrics for Low-Voltage, High-Performance Oxide Thin-Film Transistors. *J. Mater. Chem. C* **2016**, *4*, 10715.
(34) Park, J. H.; Yoo, Y. B.; Lee, K. H.; Jang, W. S.; Oh, J. Y.; Chae, S. S.; Baik, H. K. Low-Temperature, High-Performance Solution-Processed Thin-Film Transistors with Peroxo-Zirconium Oxide Dielectric. *ACS Appl. Mater. Interfaces* **2013**, *5*, 410.
(35) Wang, B.; Guo, P.; Zeng, L.; Yu, X.; Sil, A.; Huang, W.; Leonardi, M. J.; Zhang, X.; Wang, G.; Lu, S.; Chen, Z.; Bedzyk, M. J.; Schaller, R. D.; Marks, T. J.; Facchetti, A. Expeditious, Scalable Solution Growth of Metal Oxide Films by Combustion Blade Coating for Flexible Electronics. *Proc. Natl. Acad. Sci. U.S.A.* **2019**, *116*, 9230.
(36) Sil, A.; Avazpour, L.; Goldfine, E. A.; Ma, Q.; Huang, W.; Wang, B.; Bedzyk, M. J.; Medvedeva, J. E.; Facchetti, A.; Marks, T. J. Structure−Charge Transport Relationships in Fluoride-Doped Amorphous Semiconducting Indium Oxide: Combined Experimental and Theoretical Analysis. *Chem. Mater.* **2019**, *32*, 805.
(37) Moon, E. J.; Xie, Y.; Laird, E. D.; Keavney, D. J.; Li, C. Y.; May, S. J. Fluorination of Epitaxial Oxides: Synthesis of Perovskite Oxyfluoride Thin Films. *J. Am. Chem. Soc.* **2014**, *136*, 2224.

(38) Mori, T.; Kajihara, K.; Kanamura, K.; Toda, Y.; Hiramatsu, H.; Hosono, H. Indium-Based Ultraviolet-Transparent Electroconductive Oxyfluoride Inof: Ambient-Pressure Synthesis and Unique Electronic Properties in Comparison with In2o3. *J. Am. Chem. Soc.* **2013**, *135*, 13080.
(39) Paek, M.-K.; Lindberg, D.; Pak, J.-J. Solubility Limit of Nitrogen in Fe−Cr−C−N Alloy Melt under Reduced N2 Partial Pressure. *Vacuum* **2020**, *182*, 109726.
(40) Jood, P.; Male, J. P.; Anand, S.; Matsushita, Y.; Takagiwa, Y.; Kanatzidis, M. G.; Snyder, G. J.; Ohta, M. Na Doping in Pbte: Solubility, Band Convergence, Phase Boundary Mapping, and Thermoelectric Properties. *J. Am. Chem. Soc.* **2020**, *142*, 15464.
(41) Moulder, J. F.; Chastain, J. *Handbook of X-ray Photoelectron Spectroscopy : A Reference Book of Standard Spectra for Identification and Interpretation of Xps Data*; Physical Electronics Division Perkin-Elmer Corp., 1992.
(42) Wang, B.; Zeng, L.; Huang, W.; Melkonyan, F. S.; Sheets, W. C.; Chi, L.; Bedzyk, M. J.; Marks, T. J.; Facchetti, A. Carbohydrate-Assisted Combustion Synthesis to Realize High-Performance Oxide Transistors. *J. Am. Chem. Soc.* **2016**, *138*, 7067.
(43) Wang, Y.; Zahid, F.; Wang, J.; Guo, H. Structure and Dielectric Properties of Amorphous High-Koxides: Hfo2, Zro2, and Their Alloys. *Phys. Rev. B: Condens. Matter Mater. Phys.* **2012**, *85*, 224110.
(44) Lombardo, S.; Stathis, J. H.; Linder, B. P.; Pey, K. L.; Palumbo, F.; Tung, C. H. Dielectric Breakdown Mechanisms in Gate Oxides. *J. Appl. Phys.* **2005**, *98*, 121301.
(45) Zeumault, A.; Subramanian, V. Mobility Enhancement in Solution-Processed Transparent Conductive Oxide Tfts Due to Electron Donation from Traps in High-Kgate Dielectrics. *Adv. Funct. Mater.* **2016**, *26*, 955.
(46) Luo, Y.-R. *Comprehensive Handbook of Chemical Bond Energies*; CRC Press, 2007.
(47) Huang, W.; Zeng, L.; Yu, X.; Guo, P.; Wang, B.; Ma, Q.; Chang, R. P. H.; Yu, J.; Bedzyk, M. J.; Marks, T. J.; Facchetti, A. Metal Oxide Transistors Via Polyethylenimine Doping of the Channel Layer: Interplay of Doping, Microstructure, and Charge Transport. *Adv. Funct. Mater.* **2016**, *26*, 6179.
(48) Kim, C. S.; Jo, S. J.; Lee, S. W.; Kim, W. J.; Baik, H. K.; Lee, S. J. Surface-Modified High-K Oxide Gate Dielectrics for Low-Voltage High-Performance Pentacene Thin-Film Transistors. *Adv. Funct. Mater.* **2007**, *17*, 958.
(49) Seo, J.-S.; Jeon, J.-H.; Hwang, Y. H.; Park, H.; Ryu, M.; Park, S.-H. K.; Bae, B.-S. Solution-Processed Flexible Fluorine-Doped Indium Zinc Oxide Thin-Film Transistors Fabricated on Plastic Film at Low Temperature. *Sci. Rep.* **2013**, *3*, 2085.
(50) Ceresoli, D.; Vanderbilt, D. Structural and Dielectric Properties of Amorphouszro2andhfo2. *Phys. Rev. B: Condens. Matter Mater. Phys.* **2006**, *74*, 125108.
(51) Shannon, R. D. Revised Effective Ionic-Radii and Systematic Studies of Interatomic Distances in Halides and Chalcogenides. *Acta Crystallogr., Sect. A: Cryst. Phys., Diffr., Theor. Gen. Crystallogr.* **1976**, *32*, 751.
(52) Thomas, S. R.; Pattanasattayavong, P.; Anthopoulos, T. D. Solution-Processable Metal Oxide Semiconductors for Thin-Film Transistor Applications. *Chem. Soc. Rev.* **2013**, *42*, 6910.
(53) Klauk, H. Organic Thin-Film Transistors. *Chem. Soc. Rev.* **2010**, *39*, 2643.
(54) Ravel, B.; Newville, M. Athena, Artemis, Hephaestus: Data Analysis for X-Ray Absorption Spectroscopy Using Ifeffit. *J. Synchrotron Radiat.* **2005**, *12*, 537.
(55) Kresse, G.; Hafner, J. Ab Initio molecular Dynamics for Liquid Metals. *Phys. Rev. B: Condens. Matter Mater. Phys.* **1993**, *47*, 558.
(56) Kresse, G.; Hafner, J. Ab Initio Molecular-Dynamics Simulation of the Liquid-Metal-Amorphous-Semiconductor Transition in Germanium. *Phys. Rev. B: Condens. Matter Mater. Phys.* **1994**, *49*, 14251.
(57) Kresse, G.; Furthmüller, J. Efficiency of Ab-Initio Total Energy Calculations for Metals and Semiconductors Using a Plane-Wave Basis Set. *Comput. Mater. Sci.* **1996**, *6*, 15.
(58) Kresse, G.; Furthmüller, J. Efficient Iterative Schemes for Ab Initiototal-Energy Calculations Using a Plane-Wave Basis Set. *Phys. Rev. B: Condens. Matter Mater. Phys.* **1996**, *54*, 11169.
(59) Hohenberg, P.; Kohn, W. Inhomogeneous Electron Gas. *Phys. Rev.* **1964**, *136*, B864.
(60) Kohn, W.; Sham, L. J. Self-Consistent Equations Including Exchange and Correlation Effects. *Phys. Rev.* **1965**, *140*, A1133.
(61) Perdew, J. P.; Burke, K.; Ernzerhof, M. Generalized Gradient Approximation Made Simple. *Phys. Rev. Lett.* **1996**, *77*, 3865.
(62) Perdew, J. P.; Burke, K.; Ernzerhof, M. Generalized Gradient Approximation Made Simple [Phys. Rev. Lett. 77, 3865 (1996)]. *Phys. Rev. Lett.* **1997**, *78*, 1396.
(63) Blöchl, P. E. Projector Augmented-Wave Method. *Phys. Rev. B: Condens. Matter Mater. Phys.* **1994**, *50*, 17953.
(64) Kresse, G.; Joubert, D. From Ultrasoft Pseudopotentials to the Projector Augmented-Wave Method. *Phys. Rev. B: Condens. Matter Mater. Phys.* **1999**, *59*, 1758.
(65) Heyd, J.; Peralta, J. E.; Scuseria, G. E.; Martin, R. L. Energy Band Gaps and Lattice Parameters Evaluated with the Heyd-Scuseria-Ernzerhof Screened Hybrid Functional. *J. Chem. Phys.* **2005**, *123*, 174101.
(66) Heyd, J.; Scuseria, G. E.; Ernzerhof, M. Hybrid Functionals Based on a Screened Coulomb Potential. *J. Chem. Phys.* **2003**, *118*, 8207.
(67) Momma, K.; Izumi, F. Vesta 3for Three-Dimensional Visualization of Crystal, Volumetric and Morphology Data. *J. Appl. Crystallogr.* **2011**, *44*, 1272.

## Recommended by ACS

**Fluoride Doping in Crystalline and Amorphous Indium Oxide Semiconductors**

Aritra Sil, Tobin J. Marks, *et al.*
MARCH 24, 2022
CHEMISTRY OF MATERIALS

**Effect of Atomic Layer Deposition Temperature on the Growth Orientation, Morphology, and Electrical, Optical, and Band-Structural Properties of ZnO and ...**

Kyung-Mun Kang and Hyung-Ho Park
DECEMBER 07, 2017
THE JOURNAL OF PHYSICAL CHEMISTRY C

**Structure–Charge Transport Relationships in Fluoride-Doped Amorphous Semiconducting Indium Oxide: Combined Experimental and Theoretical Analysis**

Aritra Sil, Tobin J. Marks, *et al.*
DECEMBER 20, 2019
CHEMISTRY OF MATERIALS

**Fabrication of Fluorite-Type Fluoride Ba0.5Bi0.5F2.5 Thin Films by Fluorination of Perovskite BaBiO3 Precursors with Poly(vinylidene fluoride)**

Akira Chikamatsu, Tetsuya Hasegawa, *et al.*
OCTOBER 12, 2018
ACS OMEGA

**Get More Suggestions >**



https://doi.org/10.1021/acsami.1c22853
*ACS Appl. Mater. Interfaces* 2022, 14, 12340−12349